INTERNATIONAL JOURNAL FOR NUMERICAL METHODS IN FLUIDS
Int. J. Numer. Meth. Fluids **26**: 1085–1105 (1998)

ADAPTIVE HYBRID (PRISMATIC–TETRAHEDRAL) GRIDS FOR INCOMPRESSIBLE FLOWS

ALICE J. CHEN[a] AND YANNIS KALLINDERIS[b,*]

[a] *Department of Aeronautics, United States Air Force Academy, Colorado Springs, CO 80840, USA*
[b] *Department of Aerospace Engineering and Engineering Mechanics, The University of Texas at Austin, Austin TX 78712, USA*

SUMMARY

Hybrid grids consisting of prisms and tetrahedra are employed for the solution of the 3-D Navier–Stokes equations of incompressible flow. A pressure correction scheme is employed with a finite volume–finite element spatial discretization. The traditional staggered grid formulation has been substituted with a collocated mesh approach which uses fourth-order artificial dissipation. The hybrid grid is refined adaptively in local regions of appreciable flow variations. The scheme operations are performed on an edge-wise basis which unifies treatment of both types of grid elements. The adaptive method is employed for incompressible flows in both single and multiply-connected domains. © 1998 John Wiley & Sons, Ltd.

KEY WORDS: adaptive; hybrid grids; incompressible; Navier–Stokes; finite volume; pressure correction; 3-D

1. INTRODUCTION

During the past two decades a significant number of numerical algorithms have been developed for the solution of the incompressible Navier–Stokes equations and a few major issues have arisen from these studies. The lack of a pressure term in the continuity equation makes the momentum equations with the divergence-free constraint more difficult to solve [1]. Furthermore, non-staggered spatial discretization of the pressure and velocity fields may produce oscillatory solutions, which has traditionally led to the use of staggered grids [2,3]. However, the use of staggered grids can be quite complex for locally refined grids which also employ mixed elements. Thus, the employment of a non-staggered grid which has velocity and pressure values stored at the same locations affords more flexibility, but requires artificial dissipation to eliminate oscillations.

A final issue regarding numerical methods for incompressible flow relates to the topology of the computational grid, especially for three-dimensional bodies. The generation of a structured hexahedral grid for complex geometries can be difficult [4]. Unstructured tetrahedral grids provide flexibility in three-dimensional grid generation because they can cover complicated topologies more easily than the hexahedral meshes. Substantial progress is currently being made in large scale viscous flow computations on complex three-dimensional geometries using compressible flow solvers. However, there has been very little analogous work using incompressible viscous flow solvers. The proposed mesh methodology [5,6] provides an alternative

* Correspondence to: Department of Aerospace Engineering and Engineering Mechanics, The University of Texas at Austin, Austin, TX 78712, USA

CCC 0271–2091/98/091085–21$17.50

Received 21 February 1996
Revised 16 May 1997

approach to generate suitable grids for Navier–Stokes computations through the use of prismatic elements, as shown in Figure 1. The prisms permit the use of sufficient grid clustering in the normal direction, as well as flexibility in covering complex surfaces using their triangular faces. Prismatic data structures also require considerably less memory storage compared with tetrahedral data structures [7]. The hybrid mesh incorporates both prismatic and tetrahedral elements [5]. The prismatic cells are used close to the body surfaces and fill only a small fraction of the computational domain. Since unstructured grids have the capability to fill irregular regions, the remaining portion of the domain is tessellated with tetrahedra which are generated starting from the triangulation of the outermost surface of the prismatic region.

A popular category of algorithms used to solve incompressible flows is the pressure correction method. The usual computational procedure for pressure correction methods is to assume an initial pressure and velocity field, and then iterate until the continuity equation is satisfied. The present work focuses on the application of an edge-based pressure correction method using adaptive hybrid grids for the solution of the incompressible Navier–Stokes equations. The employment of adaptive hybrid grids introduces the following issues which are examined in the present work:

- Creation of a single algorithm for grids of mixed elements (prisms–tetrahedra).
- Stability of the pressure correction method with adaptive grids consisting of mixed elements.
- Stability of the pressure correction method in the presence of two different types of interfaces; the prismatic–tetrahedral interface, as well as the interfaces between different embedded grids.
- Effect of the various interfaces on solution accuracy.
- Employment of explicit artificial dissipation for stability instead of the more traditional approach of staggered grids.

The results presented discretize the flow domain using a non-staggered hybrid grid, comprising of both prismatic and tetrahedral elements. The implementation of edge-based operations makes the use of these hybrid elements transparent to the algorithm. Explicit artificial dissipation is shown to eliminate oscillations incurred by not using the staggered grid approach. Additionally, a hybrid grid adaptation scheme is implemented using local mesh refinement. The pressure correction method is shown to be stable in the presence of the prism–tetrahedra interface, as well as the interfaces between different embedded grids. The local adaptation scheme is also shown to be advantageous, yielding accurate results with reduced computing resources.

2. THE PRESSURE CORRECTION METHOD

The governing Navier–Stokes equations are normalized by a characteristic length (L) and the freestream speed (U_∞). The terms in the equations are rearranged into inviscid, viscous, and source terms. The non-dimensional Navier–Stokes equations in three dimensions can be written in Cartesian co-ordinates in differential form:

$$\frac{\partial \mathbf{U}}{\partial t} + \frac{\partial (\mathbf{F_I} - \mathbf{F_V})}{\partial x} + \frac{\partial (\mathbf{G_I} - \mathbf{G_V})}{\partial y} + \frac{\partial (\mathbf{H_I} - \mathbf{H_v})}{\partial z} = S. \tag{1}$$

The state vector $\mathbf{U}$, the convective flux vectors $\mathbf{F_I}$, $\mathbf{G_I}$, $\mathbf{H_I}$, the viscous flux vectors $\mathbf{F_V}$, $\mathbf{G_V}$, $\mathbf{H_V}$, and the source term $\mathbf{S}$ are expressed in terms of the non-dimensional primitive variables.

An explicit–implicit marching scheme is adopted for the time integration of equations (1). The velocity values are marched in time with a forward Euler scheme [8]. The continuity equation is formulated implicitly with the velocity values considered at time level $(n+1)$. Specifically, the corresponding semi-discrete system is written as follows, where the superscripts denote the time levels.

$$\mathbf{U}^T = (0 \quad u^{n+1} \quad v^{n+1} \quad w^{n+1}), \tag{2}$$

$$\mathbf{F}_\mathbf{I}^T = (u^{n+1} \quad u^n u^n \quad u^n v^n \quad u^n w^n), \tag{3}$$

$$\mathbf{G}_\mathbf{I}^T = (v^{n+1} \quad v^n u^n \quad v^n v^n \quad v^n w^n), \tag{4}$$

$$\mathbf{H}_\mathbf{I}^T = (w^{n+1} \quad w^n u^n \quad w^n v^n \quad w^n w^n), \tag{5}$$

$$\mathbf{F}_\mathbf{V}^T = \frac{1}{Re}\left(0 \quad \frac{\partial u^n}{\partial x} \quad \frac{\partial v^n}{\partial x} \quad \frac{\partial w^n}{\partial x}\right), \tag{6}$$

$$\mathbf{G}_\mathbf{V}^T = \frac{1}{Re}\left(0 \quad \frac{\partial u^n}{\partial y} \quad \frac{\partial v^n}{\partial y} \quad \frac{\partial w^n}{\partial y}\right), \tag{7}$$

$$\mathbf{H}_\mathbf{V}^T = \frac{1}{Re}\left(0 \quad \frac{\partial u^n}{\partial z} \quad \frac{\partial v^n}{\partial z} \quad \frac{\partial w^n}{\partial z}\right), \tag{8}$$

$$\mathbf{S}^T = \left(0 \quad -\frac{\partial P^{n+1}}{\partial x} \quad -\frac{\partial P^{n+1}}{\partial y} \quad -\frac{\partial P^{n+1}}{\partial z}\right). \tag{9}$$

The Reynolds number, Re, is equal to $\rho_\infty U_\infty L/\mu_\infty$, where μ_∞ is the freestream viscosity.

Equations (1)–(9) cannot be solved directly due to the implicit treatment of the pressure term. An auxiliary velocity vector $\mathbf{U}'^T = (0 \;\; u' \;\; v' \;\; w')$ is introduced, and is written in a similar non-dimensional state vector formulation used previously:

$$\frac{\partial \mathbf{U}'}{\partial t} + \frac{\partial(\mathbf{F}_\mathbf{I} - \mathbf{F}_\mathbf{V})}{\partial x} + \frac{\partial(\mathbf{G}_\mathbf{I} - \mathbf{G}_\mathbf{V})}{\partial y} + \frac{\partial(\mathbf{H}_\mathbf{I} - \mathbf{H}_\mathbf{v})}{\partial z} = 0. \tag{10}$$

However, the auxiliary velocity field, $\vec{u}'$, does not satisfy the continuity equation. Subtracting Equation (10) from the momentum Equations (1)–(9) and rewriting in primitive variables, yields:

$$\vec{u}^{(n+1)} - \vec{u}' = [\nabla p^{(n+1)}]\Delta t. \tag{11}$$

Introducing a scalar potential, ϕ, such that

$$\vec{u}^{(n+1)} - \vec{u}' = -\nabla\phi, \tag{12}$$

the following equation for pressure can be obtained:

$$p^{(n+1)} = \frac{1}{\Delta t}\,\phi. \tag{13}$$

Finally, taking the divergence of each side of Equation (12) and considering the continuity equation, the following pressure correction Poisson equation is obtained. Finite element discretization of the Poisson equation is used.

$$\nabla^2\phi = \nabla \cdot \vec{u}'. \tag{14}$$

Using the ϕ values obtained by Equation (14), we can correct the velocity and pressure fields using Equations (12) and (13) as follows:

$$\vec{u}^{(n+1)} = \vec{u}' - \nabla\phi, \tag{15}$$

$$p^{(n+1)} = \frac{1}{\Delta t}\,\phi. \tag{16}$$

The overall solution procedure corresponding to marching by one time step is summarized as follows:

1. Calculate the auxiliary velocity vector $\vec{u}'$ from (10) using $\vec{u}^{(n)}$ values.
2. Solve the pressure correction Poisson Equation (14) and obtain the ϕ values.
3. Correct the pressure and velocity at time step $n+1$ using Equations (15) and (16).

3. FINITE VOLUME SPATIAL INTEGRATION FOR MIXED ELEMENTS

The present 3-D numerical method uses a non-staggered cell-vertex scheme. In addition, a node-centered *dual cell* is defined, which represents the control volume over which the integral averages of the governing equations are evaluated. The two-dimensional analogy of defining node-centered dual cells for different situations in a triangular-quadrilateral hybrid mesh is illustrated in Figure 2. Node-centered dual cells are defined by connecting the mid-points of the edges and centroids of the triangular and/or quadrilateral faces that share the node. Node-centered dual cells for a three-dimensional hybrid grid are constructed along similar lines, using the centroids of faces and cells associated with each node.

3.1. Spatial integration

The Navier–Stokes equations of incompressible viscous flow are given in integral form for a bounded three-dimensional domain Ω as follows:

$$\int_\Omega \left[\frac{\partial \mathbf{U}}{\partial t} + \left(\frac{\partial(\mathbf{F_I}-\mathbf{F_V})}{\partial x} + \frac{\partial(\mathbf{G_I}-\mathbf{G_V})}{\partial y} + \frac{\partial(\mathbf{H_I}-\mathbf{H_V})}{\partial z}\right)\right] \mathrm{d}\Omega = \int_\Omega \mathbf{S}\,\mathrm{d}\Omega. \tag{17}$$

The state, flux and source vectors have been previously defined in Equations (2)–(9).

In the finite volume approach, the volume integral containing the spatial derivatives of the inviscid and viscous flux vectors in Equation (17) is transformed to a surface integral using the divergence theorem.

$$\int_\Omega \left[\frac{\partial \mathbf{U}}{\partial t} - \mathbf{S}\right] \mathrm{d}\Omega + \int_{\partial\Omega} [(\mathbf{F_I}-\mathbf{F_V})n_x + (\mathbf{G_I}-\mathbf{G_V})n_y + (\mathbf{H_I}-\mathbf{H_V})n_z]\,\mathrm{d}S = 0. \tag{18}$$

The surface integral of Equation (18), is rewritten in discrete form on an edge-wise basis,

$$\sum_e [(\mathbf{F_I}-\mathbf{F_V})S_x + (\mathbf{G_I}-\mathbf{G_V})S_y + (\mathbf{H_I}-\mathbf{H_V})S_z]_e, \tag{19}$$

where the summation is over all the edges; S_x, S_y, S_z are the area-projections of the dual faces associated with each edge e in the corresponding co-ordinate directions. The flux vectors are required at the center of the edge e and their values are obtained by averaging the values at the two nodes of each edge. Since the flux summation is over the edges, it is transparent to the scheme whether a node lies in the tetrahedral region, prismatic region, or at the interface. The viscous flux vectors $\mathbf{F_V}$, $\mathbf{G_V}$ and $\mathbf{H_V}$ of Equation (18) contain the gradients of the velocities that need to be calculated at the edge centers. For this calculation, another conceptual dual cell is

used. The two-dimensional analogy of this cell is shown in Figure 3. The edge-centered dual cell is composed of all the cells which share the edge. Once the first-order derivatives of the terms $\mathbf{F_V}$, $\mathbf{G_V}$ and $\mathbf{H_V}$ have been calculated, the viscous terms are evaluated at the nodes.

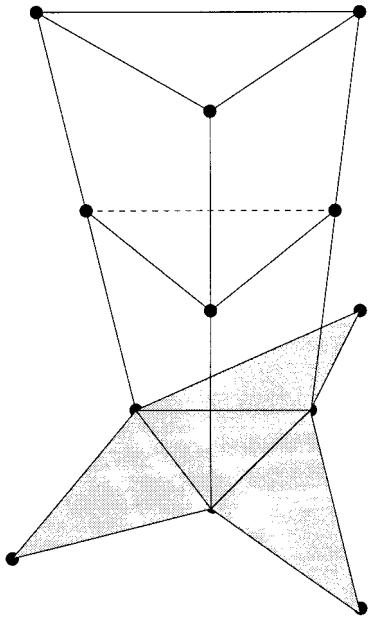

Figure 1. Semi-unstructured prismatic topology. (The unstructured boundary surface is shaded.)

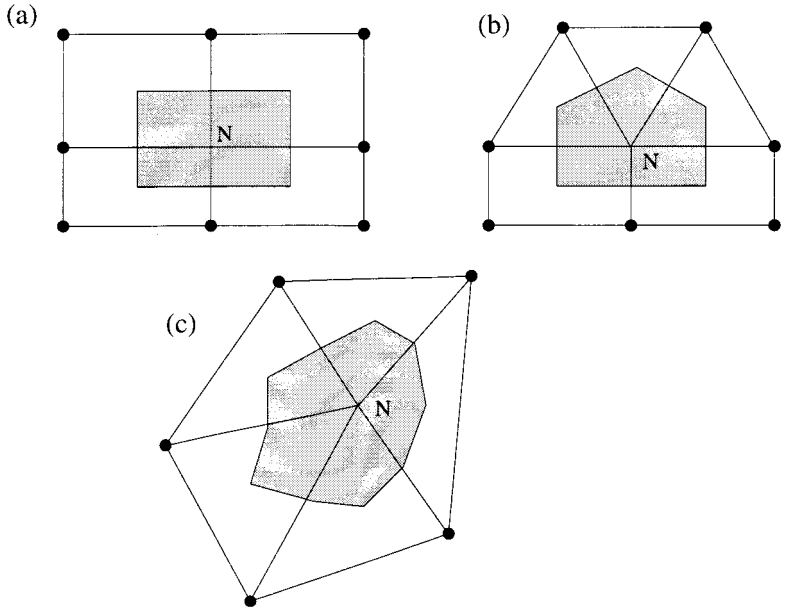

Figure 2. 2-D analogies for node-centered dual areas in the (a) prismatic region; (b) tetrahedral–prismatic interface; and (c) tetrahedral region.

In the present central space and forward time differenced scheme, a combination of the convective and diffusion stability limitations is employed. Specifically,

$$\Delta t = \frac{\omega \cdot V_i}{|u_i S_{ix}| + |v_i S_{iy}| + |w_i S_{iz}| + 2 \cdot V_i/(Re(|S_{ix}| + |S_{iy}| + |S_{iz}|))}, \tag{20}$$

where V_i is the dual volume corresponding to node i, u_i, v_i and w_i are the velocities at node i, S_{ix}, S_{iy} and S_{iz} are the projected areas of the faces of the dual cell corresponding to node i, and ω is the CFL number.

3.2. Boundary conditions

The velocity components are set equal to zero at the wall, while the derivative of the scalar potential, $\partial\phi/\partial n$, is also equal to zero. The far field boundary conditions set the velocity to be equal to the freestream velocity, and $\partial\phi/\partial n$ to be equal to zero. At symmetry boundaries, the tangential components of the velocity at the center of the boundary cell are projected to the cell faces on the symmetry boundary. Furthermore, the normal component of the velocity on a symmetry boundary is set to zero and $\partial\phi/\partial n$ is also set to zero. Note that the use of all Neumann boundary conditions for the scalar potential ϕ admits floating of the Poisson solution. Consequently, the present scheme sets ϕ equal to zero at one far field location to ensure uniqueness of the solution [9].

Implementation of the Neumann boundary conditions for the scalar potential and velocity components is complicated by the use of hybrid grids. Unlike fully structured meshes where boundary information can be easily related to neighboring nodes, hybrid meshes require careful extrapolation based on the type of boundary element incurred. When a prismatic or tetrahedral cell is on a Neumann boundary, the cell center value of ϕ is extrapolated to the center of the boundary face. This face center value is then distributed to the face nodes. The nodal distribution uses weighting factors which are inversely proportional to the distance of the face node from the face center. Therefore, the closer the face node is to the face center, the greater the distribution the face node will receive. Illustration of the extrapolation process for a tetrahedral boundary cell is shown in Figure 4.

3.3. Artificial dissipation

Central space differencing schemes are susceptible to oscillatory modes in the velocity field. Furthermore, odd–even decoupling of the solution may appear in the pressure field when a non-staggered type of mesh is employed. To stabilize the calculations for high Reynolds number flows, artificial dissipation is often used. In the present work, a fourth-order smoothing term is added explicitly to the momentum equations [10]. The smoothing operator is edge-based and cast in a form suitable for adaptive unstructured grids. Consider an edge formed by the nodes L and R. The first differences of the state vector $(\delta \mathbf{U})_2$ are evaluated as follows:

$$(\delta \mathbf{U}_L)_2 = \sum_{e=1}^{n} (\mathbf{U}_R - \mathbf{U}_L), \tag{21}$$

where e denotes the edges sharing node L. The fourth-order smoothing contribution is computed in a similar fashion. Instead of the first difference of state vectors, as used in Equation (21), a difference of the accumulated first difference over the edges sharing a node is used. The fourth-order difference is scaled by the time step at node L, Δt and the node volume, Ω_L, as follows:

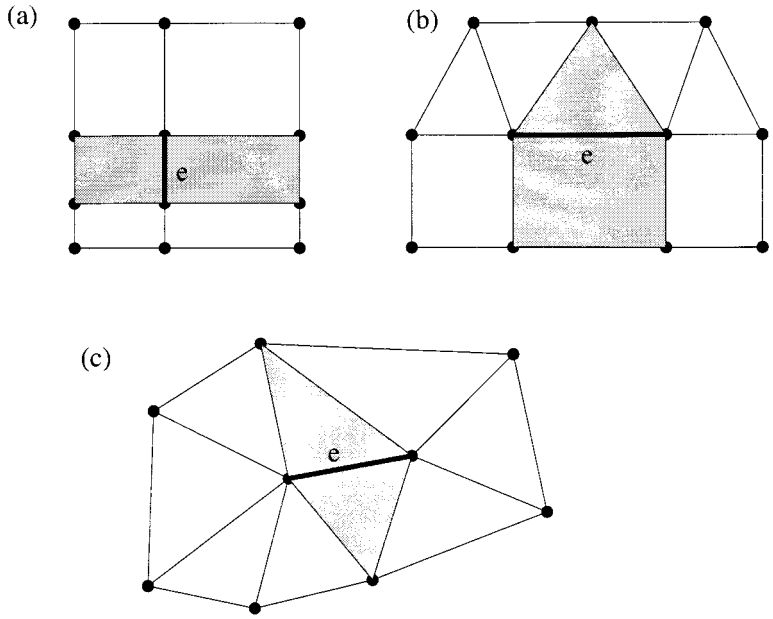

Figure 3. 2-D analogies for edge-centered dual areas in the (a) prismatic region; (b) tetrahedral–prismatic interface; and (c) tetrahedral region.

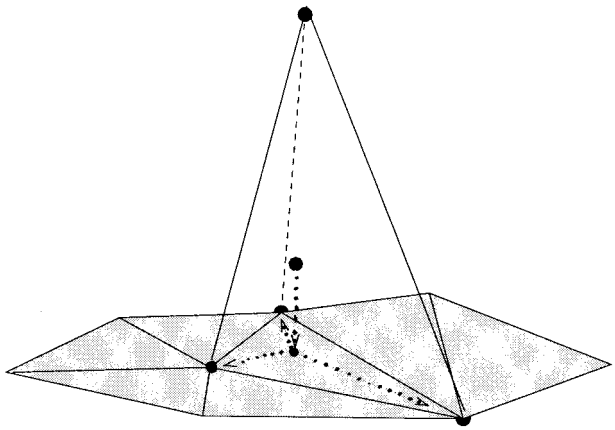

Figure 4. Illustration of far field boundary conditions for a hybrid mesh: assigning the cell center value to the tetrahedral face center, and distributing the face center value to the face nodes.

$$(\delta \mathbf{U}_L)_4 = -\sigma_4 \frac{\Delta t}{\Omega_L} \sum_{e=1}^{n} [(\delta \mathbf{U}_R)_2 - (\delta \mathbf{U}_L)_2]. \tag{22}$$

The coefficient σ_4 is the artificial dissipation factor, the value of which is empirically chosen such that the solution accuracy is not affected [11].

3.4. A priori evaluation of mesh quality

Evaluation of the mesh quality is made initially without having to solve the Navier–Stokes equations. Mesh quality estimates have been used in the past, however, these are often inappropriate for viscous type grids. In contrast, analytic field functions offer an attractive

method for evaluating the suitability of the prismatic–tetrahedral mesh, as well as spatial accuracy of the finite volume scheme. In this section, mesh qualities are evaluated by comparing the analytic results of the field function with values obtained by applying the divergence and viscous calculations of the numerical scheme to the same field function.

The divergence calculation is tested using the vector $\mathbf{U} = (x + y + z)\hat{i} + (x + y + z)\hat{j} + (x + y + z)\hat{k}$. The error of the numerical solution is defined as $\text{Error} = |(\nabla \cdot \mathbf{U}_{\text{numerical}} - \nabla \cdot \mathbf{U}_{\text{analytic}}/\nabla \cdot \mathbf{U}_{\text{analytic}})|$. Two different meshes are considered, an all-prisms grid and a hybrid mesh. Figure 5 shows the error distribution over the nodes for the two grids. It is observed that the majority of the nodes in the prismatic mesh have an error of $< 1.0\%$. The maximum error for this mesh was 1.8%. The majority of the nodes in the hybrid mesh have errors $< 0.1\%$.

The effect of grid size on accuracy is demonstrated with three prismatic meshes around a sphere. Two different types of calculations are considered. The first is the evaluation of the divergence $\nabla \cdot \mathbf{U}$ using the previous linear field function, while the second is evaluation of the Laplacian, $\nabla^2 U$, using the parabolic function $U = x^2 + y^2 + z^2$. Each coarse prism cell is subdivided into eight prism cells in order to construct the medium mesh. The fine mesh is created from the medium mesh using the same refinement principle. The RMS error distribution of the divergence and viscous calculations using the coarse, medium and fine grids are shown in Figure 6. The slope of the log–log plot for both calculations is approximately equal to two, which indicates second-order spatial accuracy.

4. ADAPTIVE HYBRID GRIDS

Adaptive embedding for the prismatic grid is accomplished by division of the triangular surface faces. The height of the prismatic cells normal to the surface faces is unaltered. This type of directional adaptation increases the lateral resolution of the grid, and does not destroy the structure of the prismatic mesh. The subdivision principle is illustrated in Figure 7. A triangle can be subdivided into two triangles (binary division) or it can be divided into four triangles (quad division). A triangular face with two or three of its edges flagged for division will be divided into four subfaces. If only one edge is flagged, division into two subfaces will occur.

Tetrahedral cells fill the portion of the domain away from the wall surfaces. The tetrahedra are refined into two, four, or eight subcells, corresponding to binary, quadtree and octree division [7]. The tetrahedral cells created by the isotropic *octree* division have an aspect ratio that is comparable with that of the parent cell, whereas the directional *binary* and *quadtree* divisions result in skewed cells. To avoid excessive grid skewness, repeated binary and quadtree divisions of tetrahedra that originated from such a refinement in a previous pass are avoided. Furthermore, to avoid sudden changes in grid size, the grid refinement algorithm limits the ratio in embedding level between neighboring cells to 2:1.

The hybrid adaptation is completed by coupling the refined prismatic and tetrahedral grids together at the interface. The feature detectors that flag the edges in the prismatic and tetrahedral regions function independently, therefore, the following situations may occur: (i) an edge on the wall surface may be flagged for refinement but its *counterpart* in the tetrahedral region may not have been flagged by the tetrahedral feature detector, and (ii) a tetrahedral edge may be flagged for refinement, but its *footprint* on the wall may not have been flagged by the prismatic feature detector. In the previous cases, mid-edge nodes (hanging) nodes will appear, which would then require special treatment by the solver. Hanging nodes are avoided by flagging both cells of a prism–tetrahedron pair at the interface, if at least one cell is flagged for division.

The success of spatial grid adaptation is dependent upon the feature detection algorithm. The feature detector needs to accurately select the regions which require finer resolution. Regions are usually selected on the basis of certain flow features [12,13,7]. For the present work, velocity gradients and velocity differences are the flow feature parameters used to

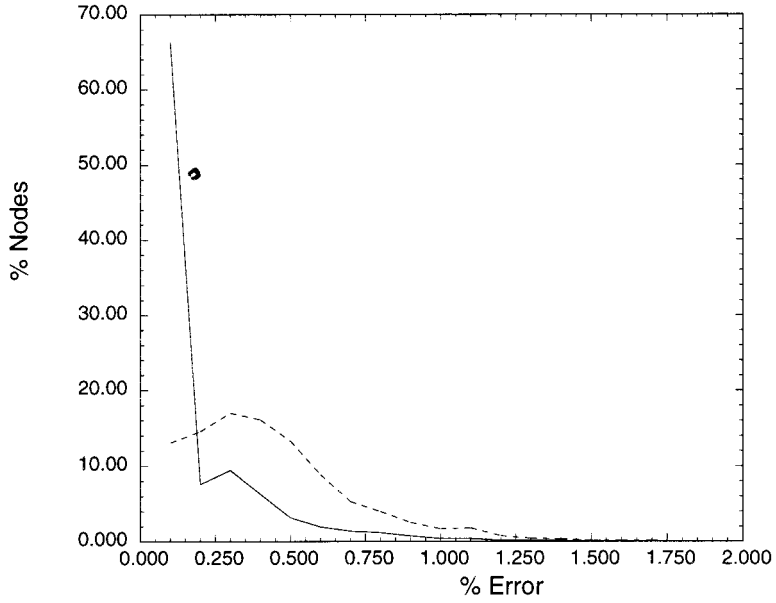

Figure 5. Numerical error distribution in the grid for calculation of the divergence of a linear analytic function around a sphere. - - -, Prismatic mesh; — hybrid mesh.

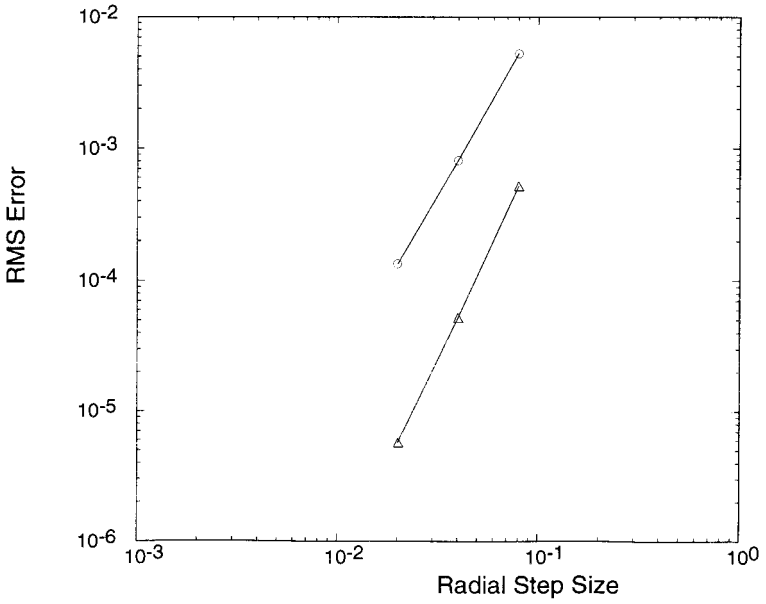

Figure 6. RMS error versus radial step size for the divergence and viscous calculations on a semi-unstructured prismatic sphere mesh. Second-order accuracy is observed. △, Divergence calculation; ○, viscous calculation.

determine where local embedding should occur. The variation in the flow parameters across the edges is monitored during the adaptive computation. The mean and standard deviation of the flow parameters across the edges are calculated for the entire flow field. If the value of the detection parameter φ at a particular edge is greater than the corresponding average value plus a fraction of its standard deviation, the edge is flagged for embedding, $\varphi_{\text{threshold}} = \varphi_{\text{mean}} + \alpha\varphi_{\text{sd}}$. This fraction, α, is called the *threshold parameter* and is determined by numerical experimentation. Additional information on this hybrid adaptation method can be found in Reference [7].

5. RESULTS

Four different geometries are considered, namely a cubic cavity, a sphere, two spheres in tandem and a circular cylinder. Different meshes are employed in order to compare accuracy and to test the robustness of the method. These adaptive grids include all-prisms, hybrid, as well as globally fine meshes.

5.1. Flow in a driven cubic cavity

Steady flow within a driven cubic cavity at $Re = 400$ is modeled. The lid (at $z = 1.0$) is moving with a steady velocity in the positive x direction, driving the flow. Due to flow symmetry, only half the cubic cavity is actually modeled. No artificial dissipation was used in this case. The grid had 2500 faces on the bottom wall with 50 prismatic layers to the top moving wall.

Velocity contours of the flow on x–z planes at $y = 0.015$ and $y = 0.5$ are shown in Figure 8. The velocity contours do not show the presence of small vortices in the corners of the cavity, however, velocity vector plots, which are not shown, indicate the vortices are present. Two velocity profiles on the symmetry plane of the cubic cavity are plotted for comparison with numerical data by Babu [14]. Figure 9 shows the u velocity versus the z co-ordinate at $x = 0.5$, and Figure 10 shows the w velocity versus the x co-ordinate at $z = 0.5$. Both plots show that the present work compares well with the numerical data from the literature.

Steady flow in the previously described cubic cavity at $Re = 400$ is calculated using coarse, adapted and globally adapted prismatic grids. All three grids have 50 prismatic layers. The number of surface faces are 994, 3068 and 3976, for the coarse, adapted and globally adapted meshes, respectively. The adapted grid was obtained from the coarse grid using the solution after 5000 iterations. No artificial dissipation was used. Figure 11 shows the signature of directional embedding of the prisms. Note that the plane shown in Figure 11 corresponds to the x–y plane of the cubic cavity in Figure 8. It is observed that the embedding is focused near the side walls of the cavity. This is due to flow deceleration near the wall boundaries. The boundary which is not totally adapted is the symmetry plane.

The w velocity versus the x location, on the symmetry plane of the cubic cavity at $z = 0.5$, is plotted in Figure 12. It shows that the coarse grid gives a poor solution for the w velocity, yet the locally adapted grid yields the same accuracy as the globally adapted grid. In this test case, there is 55% CPU time savings using the locally adapted grid for the same solution accuracy.

5.2. Flow around a sphere

Steady flow around a sphere is calculated for several Reynolds numbers on prismatic meshes. All the grids had 1346 triangles on the surface and used a radial stretching factor of

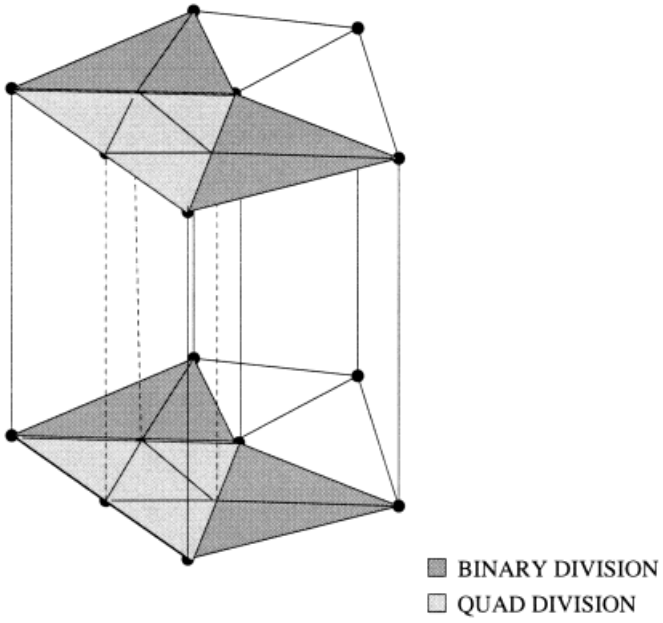

Figure 7. Local surface grid embedding for prismatic cells: shaded regions illustrate division into two (binary) and four (quad) surfaces.

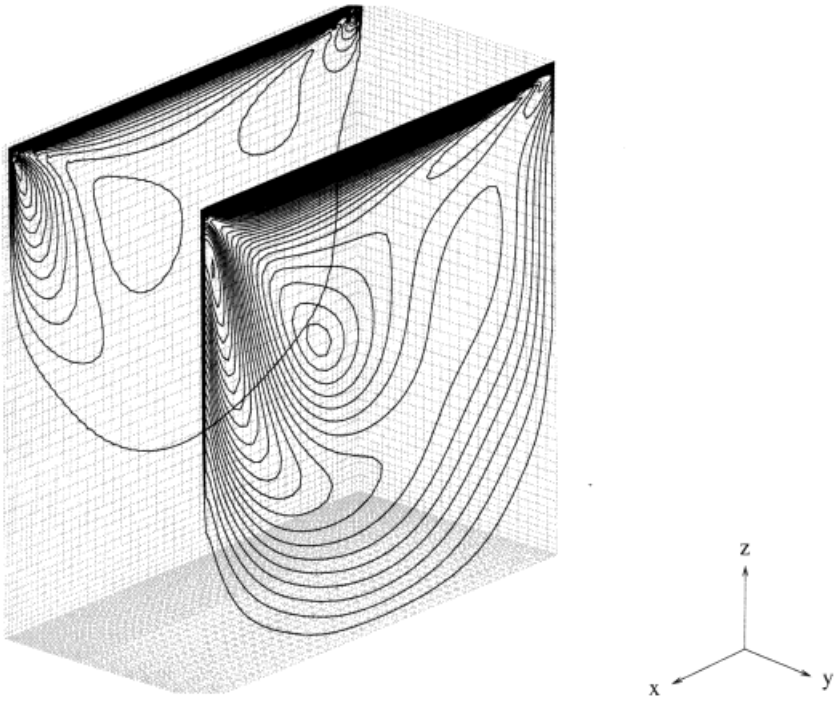

Figure 8. Velocity contours on the x–z planes in the cubic cavity at $Re = 400$, at $y = 0.015$ and 0.5. Contour lines are plotted with velocity increments equal to 0.025. The cavity lid is the top surface and is moving obliquely from right to left. The grid mesh on the bottom wall is shown, with the clustered points near walls. The grid mesh on the $x = 0$ side wall and the $y = 0$ side wall are also shown.

1.1. The convergence criterion for the maximum residual in the x-momentum equation was 10^{-5}. The artificial dissipation factor was equal to 10^{-4}.

The pathlines around the sphere are illustrated for the case of $Re = 200$ in Figures 13 and 14. Two orthogonal plane cuts are shown to illustrate the presence of the ring eddy on the rear of the sphere.

The drag coefficient variation with Reynolds number is compared with previous experiments [15,16] in Figure 15. The drag coefficient is defined by $C_d = \text{Drag}/(1/2)\,\rho_\infty U_\infty^2 A$, where A is the frontal area of the sphere (πr^2). The figure also shows the analytic solutions for Stokes and Oseen flows. It is observed that the numerical result agrees quite well with the experiments.

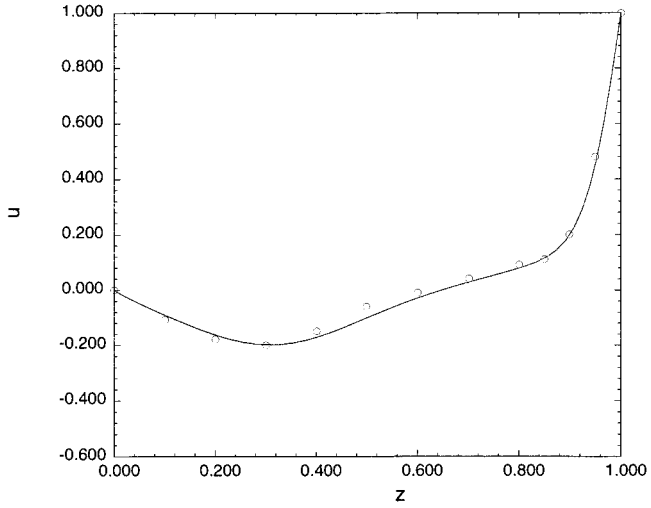

Figure 9. U velocity profile versus z on the symmetry plane at $x = 0.5$ for the driven cubic cavity flow at $Re = 400$. ○, Numerical result by Babu; —, present work (locally adapted grid).

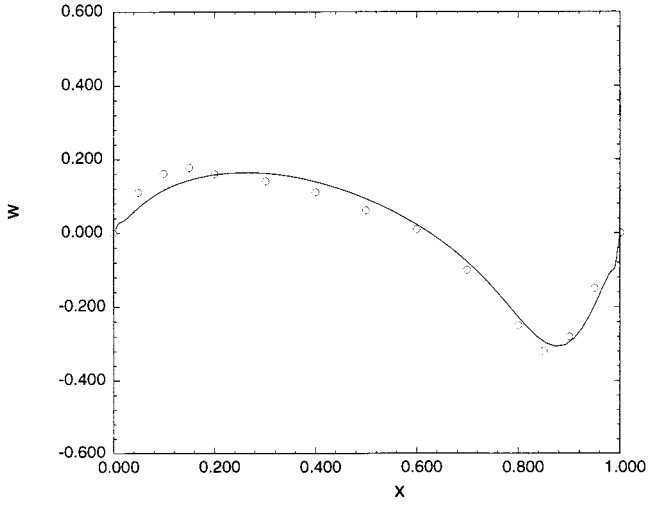

Figure 10. W velocity profile versus x on the symmetry plane at $z = 0.5$ for the driven cubic cavity at $Re = 400$. ○, Numerical result by Babu; —, present work (locally adapted grid).

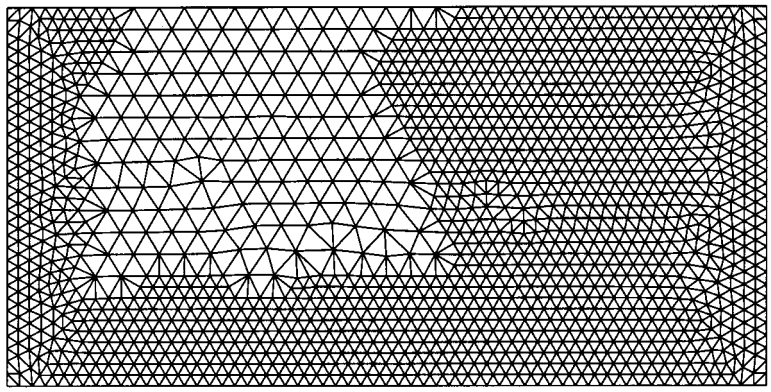

Figure 11. Signature of the prisms adaptation on the bottom wall (x–y plane) of the driven cubic cavity at $Re = 400$. Surface grid shows embedding near the cavity walls.

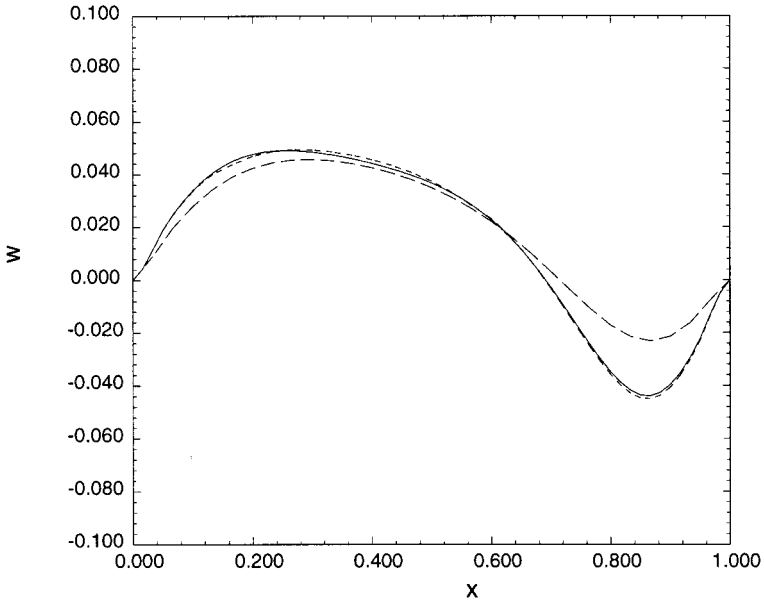

Figure 12. Effectiveness of grid adaptation. Comparison of the w velocity profile versus x on the symmetry plane at $z = 0.5$ for the driven cubic cavity at $Re = 400$. – –, Coarse grid; - - - -, locally adapted grid; —, globally fine grid.

The effect of the interface between the prisms and the tetrahedra on the solution is examined with flow around the sphere at $Re = 100$. The prismatic region was reduced so that the separation bubble would no longer lie solely in the prism region. Figure 16 shows the pathlines around the sphere. It is observed that the pathlines are smooth across the interface. Figure 17 illustrates the pressure coefficient contours on the symmetry plane. The contours are relatively smooth across the interface. The change of topology of the grid (prism–tetrahedra interface) has little effect on the solution.

Hybrid mesh adaptation is demonstrated for steady flow over a sphere at a $Re = 100$. The globally fine mesh is created by refining all the prisms of the coarse grid. The initial coarse hybrid grid, the locally adapted, as well as the globally fine mesh consist of 36 layers of prisms, with the grid step size at the wall being 0.01, and the stretching factor is 1.1. The number of

prism–tetrahedral cells for the coarse, adapted, and globally fine meshes were 11 952/35 063, 39 420/59 401 and 47 808/59 796, respectively. The artificial dissipation factor was set at 10^{-4}.

The adapted grid is shown in Figure 18 along with velocity contours around the sphere. The figure shows the tessellation on the wall surface and symmetry plane. Embedding in the tetrahedral region is focused at the rear of the sphere. The prismatic region is also directionally refined near the upstream and downstream sections of the body. This is due to the flow accelerating from the upstream stagnation point and the flow separating in the aft part of the sphere. These occurrences cause significant flow gradients in the lateral directions which are detected by the directional adaptive algorithm. The third plane cuts through the interior of the grid, normal to the symmetry plane. Despite the drastic changes in topology at the interface, the contour lines across it are relatively smooth. Figure 19 shows the pressure coefficient contours on the symmetry plane. The pressure field contours are also smooth across the prismatic–tetrahedral interface.

The distributions of the pressure coefficient and the vorticity on the surface along the equatorial plane are shown in Figures 20 and 21. The pressure coefficient solution for the adapted mesh and the fine mesh are nearly identical. However, the vorticity distribution corresponding to the adapted and fine meshes have some differences near $\theta = 60$ degrees where embedding has not occurred.

Robustness of the hybrid adapter is demonstrated in Figure 22. The maximum residual of the x-momentum equation is plotted versus time for the locally adapted and globally adapted

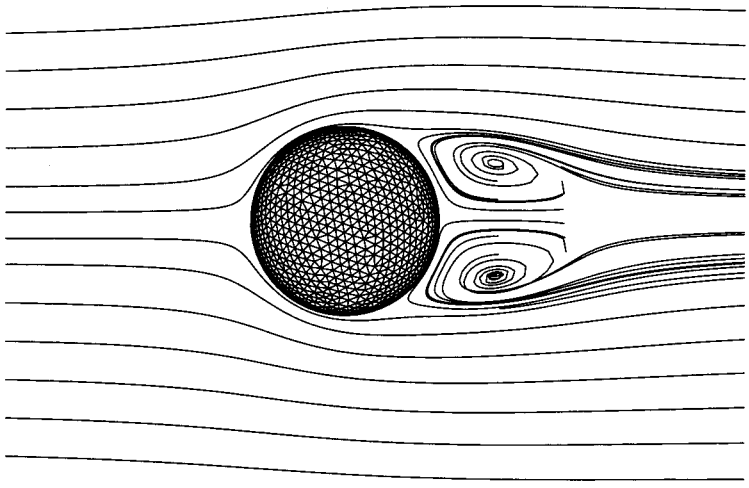

Figure 13. Pathlines on the x–z plane near a sphere at $Re = 200$.

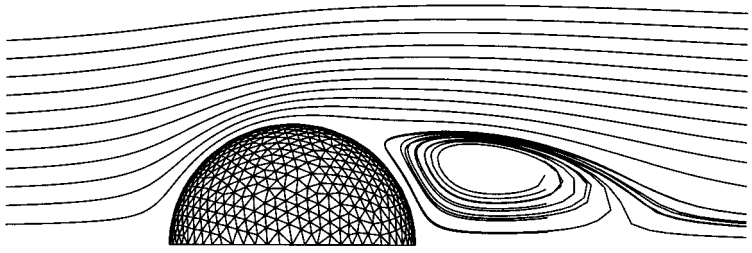

Figure 14. Pathlines on the x–y plane near a sphere at $Re = 200$.

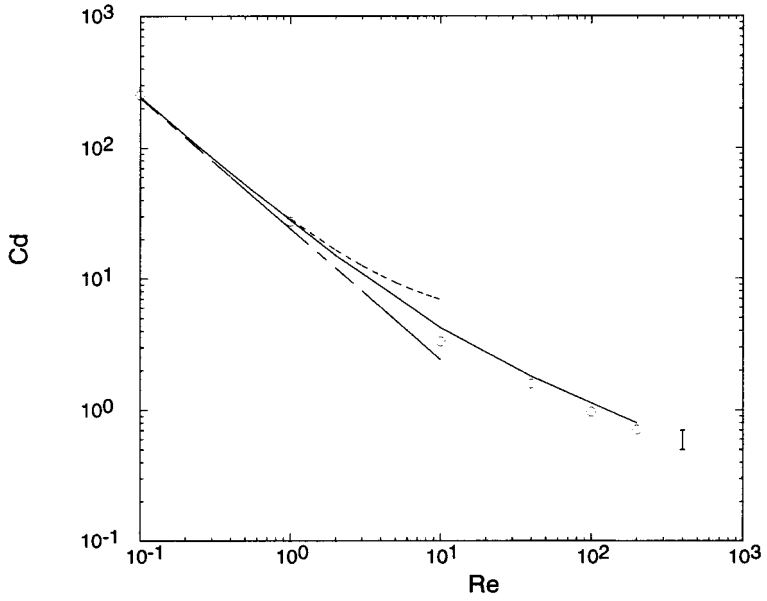

Figure 15. Drag coefficient on a sphere versus Reynolds number. Tick at lower right represents error range of experimental data. – – –, Stokes flow; - - - -, Oseen's equation; —, experimental data [7,15]; ○, present work.

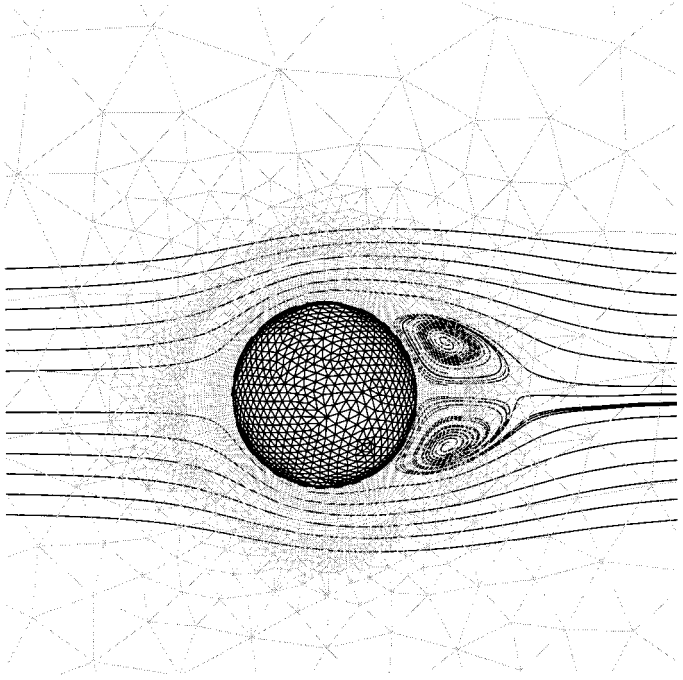

Figure 16. Effect of prism–tetrahedra interface on the solution. Pathlines near a sphere corresponding to flow of $Re = 100$ are unaffected by the change in topology of the grid.

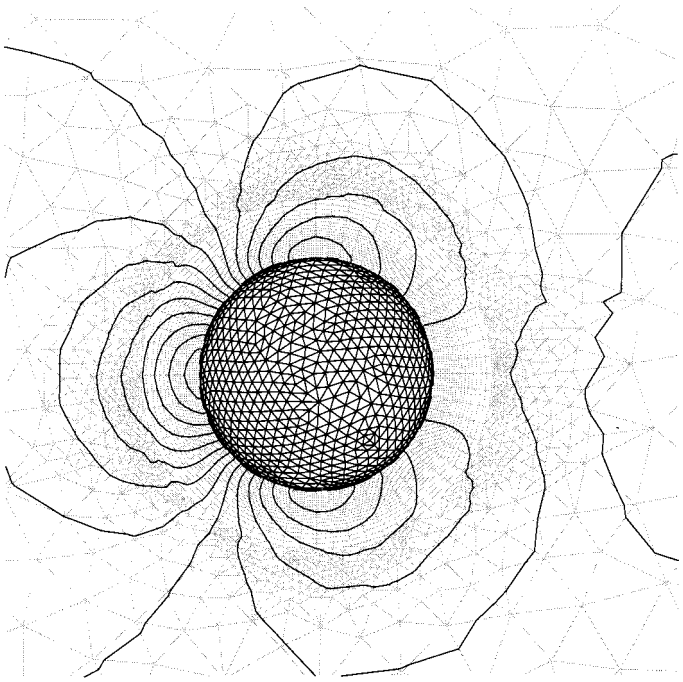

Figure 17. Effect of prism–tetrahedra interface on the solution. Pressure contours near a sphere for $Re = 100$ are relatively unaffected by the change in topology of the grid.

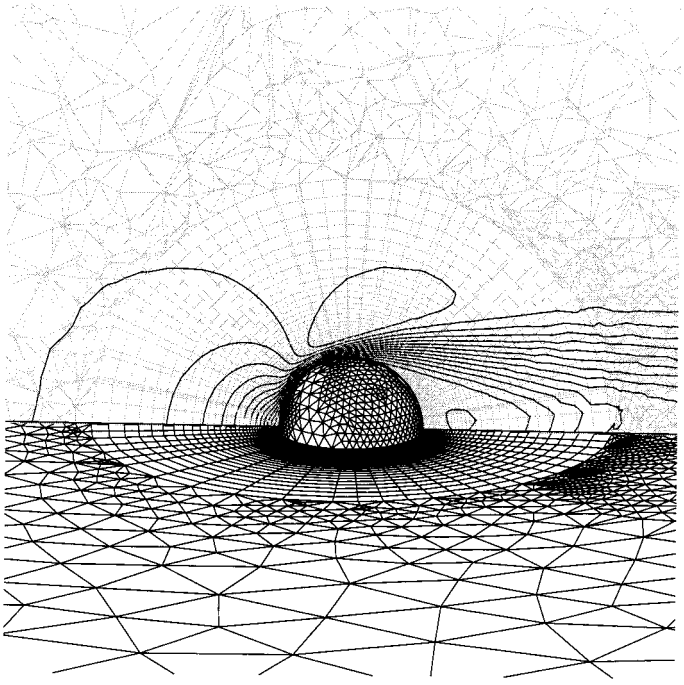

Figure 18. Adapted hybrid mesh and corresponding flow velocity contours for sphere at $Re = 100$. A view of the tessellation on the wall surface, symmetry plane and an interior equatorial plane. The hybrid grid is embedded isotropically in the tetrahedral region and directionally in the prismatic region.

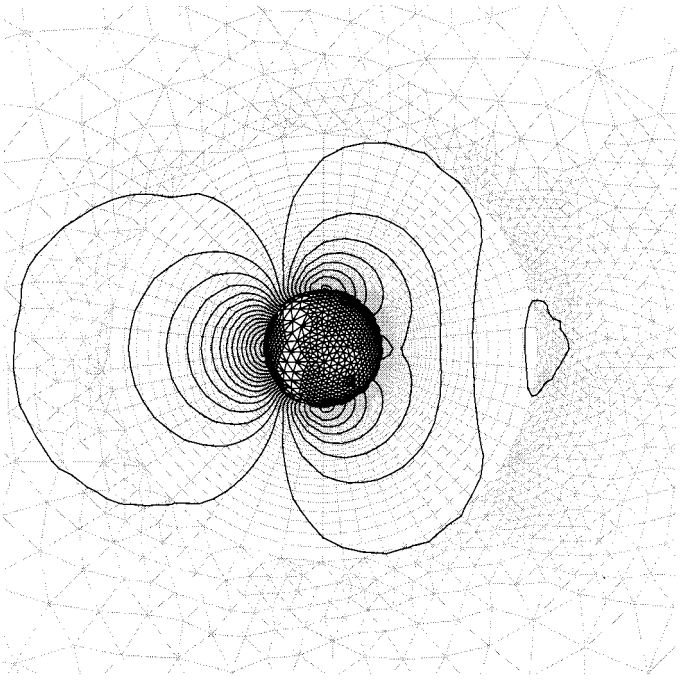

Figure 19. Adapted hybrid mesh and pressure coefficient contours for sphere at $Re = 100$. A view of the tessellation on the wall surface and symmetry plane. The hybrid grid is embedded isotropically in the tetrahedral region and directionally in the prismatic region.

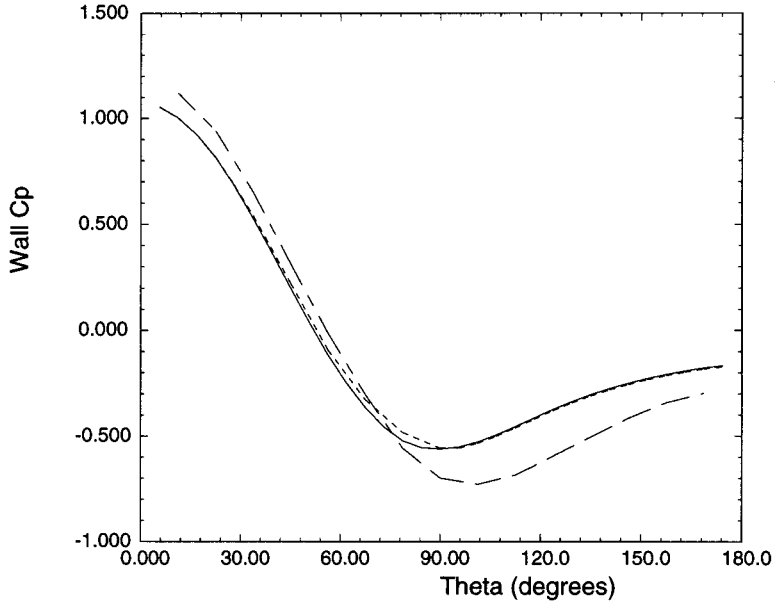

Figure 20. Pressure coefficient distribution on the surface of a sphere, at the equatorial plane, with a hybrid adapted mesh for $Re = 100$. - – -, Coarse grid; - - -, locally adapted grid; —, fine grid (globally adapted prism region).

cases. The spike in Figure 22 is due to the linearly interpolated solution from the initial coarse grid nodes to the newly created ones following adaptation. The locally adapted grid yields the same result as the globally fine with 40% less CPU time.

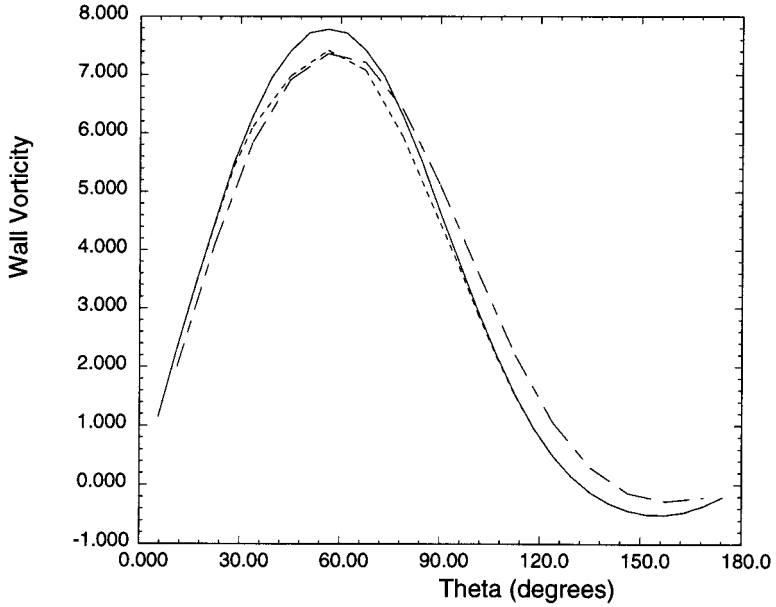

Figure 21. Vorticity distribution on the surface of a sphere, at the equatorial plane, with a hybrid adapted mesh for $Re = 100$. - – -, Coarse grid; - - -, locally adapted grid; —, fine grid (globally adapted prism region).

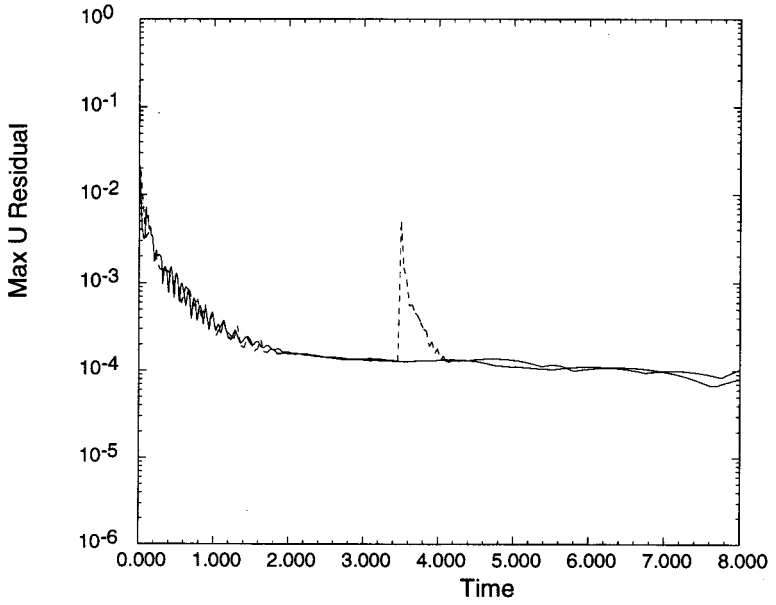

Figure 22. Demonstration of robustness of the adaptive hybrid mesh solver. Convergence history corresponding to flow around a sphere at $Re = 100$. The spike is due to the linearly interpolated solution from the initial coarse grid nodes to the newly created nodes following adaptation. - - -, locally adapted grid; —, globally fine grid.

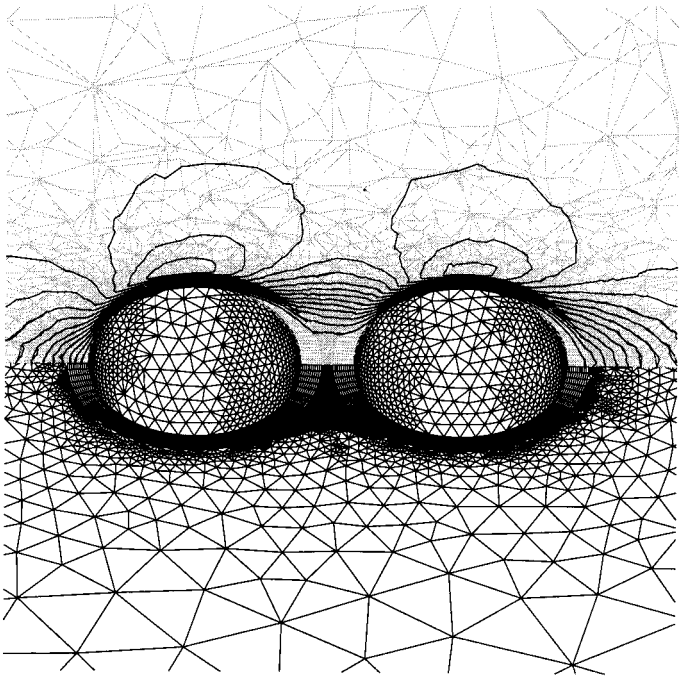

Figure 23. Adapted hybrid grid and flow velocity contours for tandem spheres at $Re = 100$. A view of the tessellation on the wall surface, symmetry plane and an interior equatorial plane. The hybrid grid is embedded isotropically in the tetrahedral region and directionally in the prismatic region.

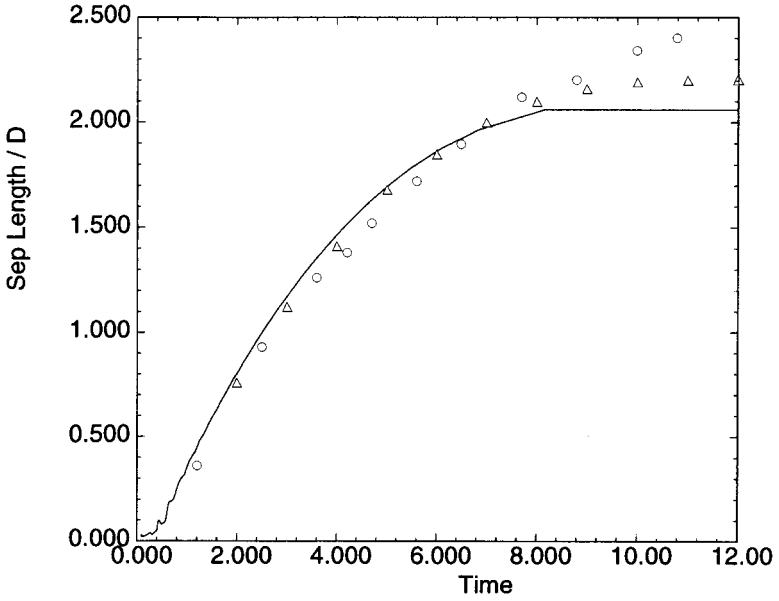

Figure 24. Growth in time of the length of the separation bubble for an impulsive start of a cylinder with $Re = 40$. △, Experiment by Coutanceau [17]; ○, experiment by Honji [18]; —, present work.

Employment of hybrid grids offers geometric flexibility. This is demonstrated in the case of a multiply-connected domain consisting of two spheres. An adaptive hybrid mesh is used to simulate the steady flow of $Re = 100$ around two spheres in a tandem (in-line with the flow) arrangement. The surface triangulation and symmetry plane of the hybrid grid are shown in Figure 23, as well as the flow velocity contours. The prismatic region shows directional adaptation on the fore and aft portions of both spheres. Embedding in the tetrahedral region is focused at the rear of the second sphere as well as the region between the two spheres. The presence of prismatic–tetrahedral grid interfaces did not affect the solution contours.

5.3. Impulsive start of a cylinder

Impulsive start of a circular cylinder which attains a steady speed corresponding to a Reynolds number of 40 is simulated with a prismatic mesh based upon an unstructured surface mesh of 1604 triangles. There were 111 layers in the prismatic mesh. Symmetry planes were defined at both ends of the cylinder. The artificial dissipation factor was equal to 10^{-4} and the CFL factor was 0.1.

The initial condition of the impulsive start simulation is potential flow [1]. The growth of the length of the separation bubble in time is shown in Figure 24. Experimental results from Coutanceau [17] and Honji [18] are shown for comparison. Results from the present work match the unsteady portion of the data, however, they slightly underpredict the length of the steady state value of the separation bubble. Note, however, that the experimental results also show a significant variation in the steady state value of the separation bubble size. Other numerical results [19] report a slight decrease in the steady state value of the separation bubble as the grid is refined. The present work found a similar trend.

6. CONCLUDING REMARKS

Employment of hybrid (prismatic–tetrahedral) grids yielded stable and accurate solutions of the incompressible Navier–Stokes equations, as demonstrated by driven cavity flow, flow over a sphere, and an impulsively started cylinder. Accuracy of the solution was not affected by the presence of prisms–tetrahedra interfaces. Solutions for the driven cavity, obtained with locally adapted grids, were basically the same as solutions yielded by the corresponding globally fine meshes. The case of the two spheres in tandem demonstrated the geometric flexibility offered by the hybrid mesh. Finally, employment of fourth-order smoothing with non-staggered grids instead of the more traditional approach of using the more complex staggered meshes, proved to yield non-oscillatory solutions.

ACKNOWLEDGMENTS

This work was supported by the Texas Advanced Technology Program (ATP) Grant # 003658-413, NSF Engineering Research Centers program grant # CDR-8721512, and NSF Grant ASC-9357677 (NYI program). The first author was also supported by the United States Air Force Academy.

REFERENCES

1. P.M. Gresho, 'Some current CFD issues relevant to the incompressible Navier–Stokes equations', *Comput. Methods Appl. Mech. Eng.*, **87**, 201–252 (1991).

2. M. Hafez and M. Soliman, 'A velocity decomposition method for viscous incompressible flow calculations, Part II', *AIAA Paper 89-1966 CP*, 1989.
3. J. Kim and P. Moin, 'Application of a fractional-step method to incompressible Navier–Stokes equations', *J. Comput. Phys.*, **59**, 308–323 (1985).
4. T.J. Baker, 'Developments and trends in three dimensional mesh generation', *Appl. Numer. Math.*, **5**, 275–304 (1989).
5. Y. Kallinderis, A. Khawaja and H. McMorris, 'Hybrid prismatic/tetrahedral grid generation for viscous flows around complex geometries', *AIAA J.*, **34**, 291–298 (1996).
6. Y. Kallinderis and S. Ward, 'Prismatic grid generation for 3-D complex geometries', *AIAA J.*, **31**, 1850–1856 (1993).
7. V. Parthasarathy and Y. Kallinderis, 'Adaptive prismatic–tetrahedral grid refinement and redistribution for viscous flows', *AIAA J.*, **34**, 707–716 (1996).
8. Y. Kallinderis and K. Nakajima, 'Finite-element method for incompressible viscous flows with adaptive hybrid grids', *AIAA J.*, **32**, 1617–1625 (1994).
9. J. Van Doormaal and G. Raithby, 'Enhancements of the SIMPLE method for predicting incompressible fluid flows', *Numer. Heat Transfer*, **7**, 147–163 (1984).
10. A. Jameson, W. Schmidt and E. Turkel, 'Numerical solutions of the Euler equations by finite-volume methods using Runge–Kutta time-stepping schemes', *AIAA Paper 81-1259*, 1981.
11. Y. Kallinderis and H. McMorris, 'Magnitude of artificial dissipation for numerical simulations, *AIAA J.*, **33**, 1526–1529 (1995).
12. Y. Kallinderis and J.R. Baron, 'A new adaptive algorithm for turbulent flows', *Comput. Fluids J.*, **21**,77–96 (1992).
13. Y. Kallinderis and P. Vijayan, 'An adaptive refinement-coarsening scheme for 3-D unstructured meshes', *AIAA J.*, **31**,1440–1447 (1993).
14. V. Babu and S.A. Korpela, 'Numerical solution of the incompressible three-dimensional Navier–Stokes equations', *Comput. Fluids*, **23**, 675–691 (1994).
15. F.W. Roos and W.W. Willmarth, 'Some experimental results on sphere and disk drag', *AIAA J.*, **9**, 285–291 (1971).
16. H. Schlichting, *Boundary-Layer Theory*, McGraw-Hill, New York, 1987.
17. M. Coutanceau and R. Bouard, 'Experimental determination of the main features of the viscous flow in the wake of a circular cylinder in uniform translation. Part 2. Unsteady flow', *J. Fluid Mech.*, **79**, 257–272 (1977).
18. H. Honji, 'Streaked flow around an oscillating circular cylinder', *J. Fluid Mech.*, **107**, 509–520 (1981).
19. W.M. Collins and S.C.R. Dennis, 'Flow past an impulsively started circular cylinder', *J. Fluid Mech.*, **60**, 105–127 (1973).

